Metal versus rare-gas ion irradiation during Ti1-xAlxN film growth by hybrid high power pulsed magnetron/dc magnetron co-sputtering using synchronized pulsed substrate bias

Grzegorz Greczynski, Jun Lu, Jens Jensen, Ivan Petrov, Joseph E. Greene, Stephan Bolz, Werner Koelker, Christoph Schiffers, Oliver Lemmer and Lars Hultman

Original Publication:

Grzegorz Greczynski, Jun Lu, Jens Jensen, Ivan Petrov, Joseph E. Greene, Stephan Bolz, Werner Koelker, Christoph Schiffers, Oliver Lemmer and Lars Hultman, Metal versus rare-gas ion irradiation during Ti1-xAlxN film growth by hybrid high power pulsed magnetron/dc magnetron co-sputtering using synchronized pulsed substrate bias, 2012, Journal of Vacuum Science & Technology. A. Vacuum, Surfaces, and Films, (30), 6, 061504.
http://dx.doi.org/10.1116/1.4750485

Metal vs. Rare-gas Ion Irradiation during $Ti_{1-x}Al_xN$ Film Growth by Hybrid HIPIMS/DCMS Co-sputtering using Synchronized Pulsed Substrate Bias

G. Greczynski,[1] J. Lu,[1] J. Jensen,[1] I. Petrov,[1,2] J.E. Greene,[1,2,3] S. Bolz,[4] W. Kölker,[4] Ch. Schiffers,[4] O. Lemmer[4] and L. Hultman[1]

[1] Department of Physics (IFM), Linköping University, SE-581 83 Linköping, Sweden

[2] Materials Science Department and Frederick Seitz Materials Research Laboratory, University of Illinois, Urbana, Illinois 61801

[3] Department of Physics, University of Illinois, Urbana, Illinois 61801, USA

[4] CemeCon AG, Adenauerstr. 20 A4, D-52146 Wűrselen, Germany

Abstract

Metastable NaCl-structure $Ti_{1-x}Al_xN$ is employed as a model system to probe the effects of metal vs. rare-gas ion irradiation during film growth using reactive high-power pulsed magnetron sputtering (HIPIMS) of Al and dc magnetron sputtering (DCMS) of Ti. The alloy film composition is chosen to be x = 0.61, near the kinetic solubility limit at the growth temperature of 500 °C. Three sets of experiments are carried out: a -60 V substrate bias is applied either continuously, in synchronous with the full HIPIMS pulse, or in synchronous only with the metal-rich-plasma portion of the HIPIMS pulse. Alloy films grown under continuous dc bias exhibit a thickness-invariant small-grain, two-phase nanostructure (wurtzite AlN and cubic $Ti_{1-x}Al_xN$) with random orientation, due primarily to intense Ar^+ irradiation leading to Ar incorporation (0.2 at%), high compressive stress (-4.6 GPa), and material loss by resputtering. Synchronizing the bias with the full HIPIMS pulse results in films which exhibit much lower stress levels (-1.8 GPa) with no measureable Ar incorporation, larger grains elongated in the growth direction, a very small volume fraction of wurtzite AlN, and random orientation. By synchronizing the bias with the metal-plasma phase of the HIPIMS pulses, energetic Ar^+ ion bombardment is greatly reduced in favor of irradiation predominantly by Al^+ ions. The resulting films are single phase with a dense competitive columnar structure, strong 111 orientation, no measureable trapped Ar concentration, and even lower stress (-0.9 GPa). Thus, switching from Ar^+ to Al^+ bombardment, while maintaining the same integrated incident ion/metal ratio, eliminates

phase separation, minimizes renucleation during growth, and reduces the high concentration of residual point defects which give rise to compressive stress.

I. INTRODUCTION

Thin films of metastable NaCl-structure $Ti_{1-x}Al_xN$ exhibiting high hardness and good high-temperature oxidation resistance[1] are used for wear protection in a wide variety of applications ranging from cutting tools to mechanical components in the aerospace industry.[2] Enhanced performance at elevated temperatures is obtained with single-phase alloy films having high AlN content. However, kinetic solid solubilities of wurtzite-structure AlN (*w*-AlN) in cubic TiN depend sensitively on film growth parameters.[3] At thermodynamic equilibrium, the solubility of AlN in TiN is low, only 2 mol% at 1000 °C (Ref.4) and 5 mol% at 2425 °C.[5] Recently, we have shown that single-phase $Ti_{1-x}Al_xN$ alloys with x up to 64 mol% can be grown using a hybrid co-sputtering technique combining high-power pulsed magnetron sputtering (HIPIMS) of Al and dc magnetron sputtering (DCMS) of Ti.[6,7] The primary ions during Al HIPIMS are Al^+.[7] Reversing the power supplies, such that the Ti target is powered by HIPIMS and Al sputtered in the DCMS mode, reduces x_{max} to ~ 40 mol%, due to bombardment by high-energy Ti^{2+} ions during the Ti HIPIMS pulse. The resulting high defect densities lead to the nucleation of wurtzite-structure AlN second-phase precipitates.

The purpose of the present research is to probe the effects of synchronous biasing during film growth by hybrid HIPIMS/DCMS co-sputtering. We use metastable $Ti_{0.39}Al_{0.61}N$ alloy films, grown at 500 °C by Al-HIPIMS/Ti-DCMS, as a model system. A -60 V bias is applied to the substrate using three different modes: (1) the bias is continuous during both HIPIMS pulses and DCMS, (2) the bias is applied in synchronous with the full HIPIMS

pulse, and (3) the bias is applied only in synchronous with the metal-rich-plasma portion of the HIPIMS pulse.

Alloy films grown under continuous dc bias are small-grain, two-phase mixtures consisting of AlN-deficient NaCl-structure $Ti_{1-x}Al_xN$ and wurtzite-structure AlN, with high compressive stress, a high concentration of trapped Ar, and no preferred orientation. Synchronizing the bias with the full HIPIMS pulse on the Al target yields films with no measureable Ar concentration, significantly lower compressive stress, larger average grain size, a smaller volume fraction of wurtzite AlN, and random texture. By synchronizing the bias with the metal plasma phase of the HIPIMS pulses, high-energy Ar^+ ion irradiation is greatly reduced in favor of irradiation predominantly by Al^+ ions. The resulting single-phase NaCl-structure $Ti_{1-x}Al_xN$ alloys have a dense competitive columnar structure with a strong 111 orientation and even lower stress.

II. EXPERIMENTAL

$Ti_{0.39}Al_{0.61}N$ films are grown in a CC800/9 CemeCon AG magnetron sputtering system[8] equipped with cast rectangular 8.8×50 cm² Ti and Al targets. Si(001) substrates, 3×1 cm^2, are mounted symmetrically with respect to the targets, which are tilted toward the substrate, resulting in a 21° angle between the substrate normal and the normal to the target. Target-to-substrate distance is 18 cm. The substrates are cleaned sequentially in acetone and isopropyl alcohol and mounted with clips such that their long sides are parallel to the long sides of the targets. The system is thoroughly degassed before deposition; we use two-hour long heating cycle, consisting of two steps. First, two resistive heaters are powered to 10 kW for 1 hour, resulting in a chamber temperature of 600 °C. Following this the heating power is reduced to 7.3 kW/heater for 1 hour (chamber temperature = 500 °C) and maintained at this level during film deposition. The system base pressure is $< 2.3\times10^{-6}$ Torr (0.3 mPa) and the

total pressure P_{tot} during deposition is 3 mTorr (0.4 Pa). Ar flow is set at 350 cm^3/min (sccm), while the N_2 flow is controlled by a feedback loop to maintain P_{tot} constant and varies between runs from 80 sccm to 72 sccm. The film growth temperature T_s is 500 °C.

The Al target is powered in HIPIMS mode (5 J/pulse, 500 Hz, 10% duty cycle), while the Ti target is operated as a conventional dc magnetron at an average power P_{dc} of 2.4 kW. As-deposited alloys films have AlN concentrations of 61±1 mol%. The AlN deposited thickness per HIPIMS pulse (200 μs) is 4.5×10^{-3} Å (~3.7×10^{-3} monolayer, ML, for 111 crystallites), while the steady-state DCMS TiN deposition rate is 1.37 Å/s. Thus, the DCMS TiN thickness during a single HIPIMS period (2 ms) is 2.7×10^{-3} Å, ~2.2×10^{-3} ML.

$Ti_{1-x}Al_xN$ films are grown with a substrate bias, V_s = -60 V, applied using one of three biasing schemes: (1) continuous bias; (2) bias applied synchronously during the full 200 μs HIPIMS pulse (between HIPIMS pulses, the substrate is at floating potential, V_f ~ -10 V); or (3) bias synchronized with the 60 μs metal-rich-plasma portion of the HIPIMS pulse beginning at 40 μs after pulse initiation (at all other times, the substrate is at V_f). The total film deposition time is 90 minutes leading to film thicknesses of (1) 1.2, (2) 1.9, and (3) 1.9 μm, as determined by scanning electron microscopy (SEM) of fracture cross-sections and confirmed by cross-sectional transmission electron microscopy (XTEM).

The substrate bias voltage and current are monitored with a Tektronix DPO4054 500 MHz bandwidth four-channel digital oscilloscope.

Time-resolved measurements of ion fluxes incident at the growing film during HIPIMS sputtering of the Al target and DCMS sputtering of the Ti target are obtained using a Hiden Analytical PSM003 mass spectrometer mounted at the substrate position as in Ref. 7. For HIPIMS operation, data are collected during 50 consecutive pulses such that the total acquisition time per data point is 1 ms. Ar, N_2, N, Al, and Ti single and multiply charged ion energy distribution functions ($IEDF_S$) are recorded with energy steps of 1 eV.

$Ti_{1-x}Al_xN$ film compositions are determined to within an uncertainty of ±1 at% by time-of-flight elastic recoil detection analysis (ToF-ERDA) employing a 36 MeV $^{127}I^{8+}$ probe beam. X-ray diffraction (XRD), together with plan-view and cross-sectional transmission electron microscopy (TEM and XTEM), are used to analyze the nano- and microstructure of as-deposited layers, while film stress σ is obtained from XRD $\sin^2\psi$ analyses.[9]

III. RESULTS

In situ ion mass spectrometry measurements reveal the presence of high-intensity energetic Al^+ fluxes incident at the substrate position during HIPIMS pulses. Ar^+, Ar^{2+}, N_2^+, and N^+ gas ions are also detected. The Al^+ ion intensity integrated over the 200-μs pulse constitutes 44.5% of the entire ion flux and is comparable to the integrated intensity of Ar^+ ions, 41.8%. However, the mean metal-ion energy is significantly higher, particularly during the time interval when the HIPIMS target current density J_T is near its maximum value (see dashed curve in Fig.1). Within the 20 μs window (t = 40 - 60 μs) for which J_T ranges from 0.41 to 0.47 A/cm^2, mean ion energies incident at the substrate plane are 11.4 eV for Al^+ *vs.* 1.8 eV for Ar^+. The flux of Al^{2+} ions is negligible (less than 0.05% of the total ion flux to the substrate), primarily due to the relatively high second-ionization potential of Al (18.83 eV)[10] and the short plasma transit time of the relatively low-mass sputter-ejected Al atoms (m_{Al} = 27 amu). Doubly-ionized Ar ions Ar^{2+} (27.63 eV)[10], 0.2% of the ion flux, have a mean energy of 10.5 eV. N_2^+ and N^+ reactive gas ions are detected with relative contributions of 10.1 and 3.4%, and mean energies of 3.7 and 7.7 eV, respectively.

Time-dependent intensities of the primary ion fluxes -- Ar^+, N_2^+, N^+, and Al^+ -- incident at the growing film during Al-HIPIMS are plotted in Figure 1 with a 20 μs resolution. Each data point at time t represents the number of ions collected during the interval from t-10 to t+10 μs. As reported previously for reactive Al-HIPIMS in Ar/N_2

mixtures,[7] the plasma is initially maintained primarily by Ar^+ and N_2^+ gas ions. The non-zero flux intensities detected at t = 0 μs in Figure 1 are due to residual ionized species from the previous pulse. The ~ 20 μs time delay before the appearance of atomic N^+ ions, together with the high N^+ mean energy (relative to N_2^+ ions), indicates that they originate primarily from N atoms sputter ejected from the target surface and ionized in the plasma. Gas-ion intensities begin to decrease after 30-40 μs due to rarefaction stemming from the high thermal and momentum load supplied by the HIPIMS target.

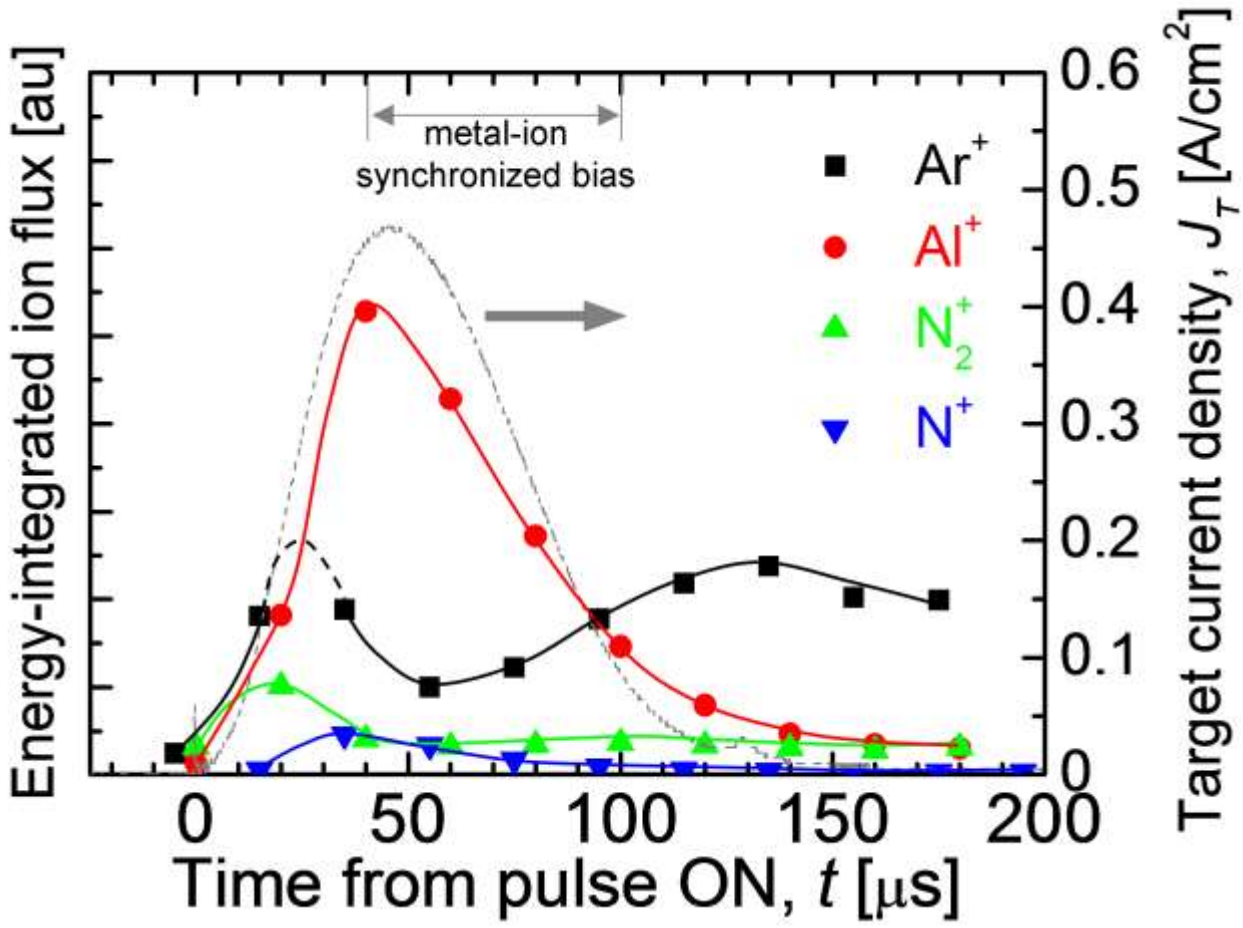

Fig.1 Time evolution of the energy-integrated flux of ions incident at the substrate: Ar^+, Al^+, N_2^+, and N^+. The target current density waveform is shown for reference.

Al has a low first ionization energy (5.986 eV)[10] and Al^+ is the dominant plasma ion from t ~ 40 to 100 μs into the pulse. Electron-impact ionization of sputter-ejected Al atoms reduces the intensity of the high-energy tail in the plasma electron energy distribution. This,

in turn, decreases the ionization probability of gas species Ar, N_2, and N which have ionization energies 15.75, 15.55, and 14.50 eV.[10] Al^+ intensity, after reaching a peak at ~50 μs, begins to decrease due to a corresponding decrease in the discharge current as the plasma becomes power-supply limited. The Ar^+ intensity again dominates during the latter half of the pulse, from $t \sim 100$ to 200 μs. N_2^+ and N^+ intensities do not fully recover due to increased target sputtering rates giving rise to efficient trapping and chemisorption of nitrogen by freshly-deposited Al atoms.

A comparison of the total ion flux (primarily Al^+ and Ar^+) during a HIPIMS pulse to the continuous ion flux (dominated by Ar^+) from dc magnetron sputtering is obtained from the time-averaged ion saturation current densities J_s measured using a 15-mm-diameter circular probe mounted at the substrate position during Al-HIPIMS and Ti-DCMS operation. J_s is 0.60 mA/cm^2 in HIPIMS and 0.35 mA/cm^2 during DCMS.

Since time-resolved ion mass spectrometry measurements in the Al-HIPIMS plasma indicate that the peak total ion count during the 200-μs HIPIMS pulse is ~8× higher than the average value obtained between the pulses, we conclude that the ion flux arising from the HIPIMS source *during* the pulse is at least an order of magnitude higher than the concurrent ion bombardment from the Ti plasma. Therefore, film growth conditions during the high-power pulses are, to a first approximation, controlled by the HIPIMS plasma.

Throughout the time between the 200 μs HIPIMS pulses, the growing film continues to be exposed to a large Ar^+ ion flux from the DCMS plasma. During these periods, Ar^+ constitutes 84% of the total ion flux to the substrate with Ti^+, N_2^+, and N^+ ions contributing 10, 4.9, and 0.1%. Mean Ar^+, Ti^+, N_2^+, and N^+ ion energies are 2.3, 4.8, 2.8, and 11.8 eV. The ion-to-metal flux ratio J_i/J_{Me} measured during Ti-DCMS operation is 3.2, essentially equal to the time-averaged value, 3.1, obtained during Al-HIPIMS/Ti-DCMS co-deposition.

The AlN concentration x in as-deposited $Ti_{1-x}Al_xN$ films is 0.61±0.01, independent of

the substrate biasing mode. The concentration of incorporated Ar is 0.2 at% for $Ti_{0.39}Al_{0.61}N$ layers grown using continuous DC bias and less than the detection limit, 0.1 at%, for the two growth modes with synchronized pulsed bias. All layers are slightly understoichiometric, with a N/Me ratio of 0.96 ±0.02. The oxygen impurity level is less than 1 at% for all three growth modes.

Significantly lower film thickness, 1.2 μm for mode (1) *vs.* 1.9 μm for modes (2) and (3), is obtained for $Ti_{0.39}Al_{0.61}N$ films deposited under continuous DC bias due to intense DCMS Ar^+ resputtering of the deposited film. This effect is reduced for films grown under pulsed bias.

Figure 2 shows typical ψ-2θ scans, obtained as a function of the sample tilt angle ψ (defined as the angle between surface normal and the diffraction plane containing the incoming and diffracted x-ray beams) and plotted on the same intensity scale, for $Ti_{1-x}Al_xN$ alloys grown using each of the three bias modes. ψ is varied from 0 to 75° in steps of 5°. The data are acquired in 0.1 degree steps and the dwell time per data point is 6 s.

In all three growth modes, diffractograms are dominated by NaCl-structure 111 and 002 film peaks. For $Ti_{0.39}Al_{0.61}N$ alloy films grown with continuous dc bias (see Fig. 2(a)), the relative 111 and 002 peak intensities do not vary with ψ. Thus, the layers are randomly oriented. In addition, the overall peak intensity is low, indicative of a small average crystallite size, consistent with TEM/XTEM results. The relaxed cubic lattice parameter a_o obtained at the strain-free tilt angle ψ^* =34.4° [Ref. 7] is 4.186 Å, significantly higher than the expected value for single-phase cubic $Ti_{1-x}Al_xN$ films with x = 0.61, a_o = 4.165 Å[7,11] (Density functional theory calculations yield 4.164 Å).[12] This suggests that films grown in bias mode (1) are two-phase mixtures consisting of AlN-deficient $Ti_{1-x}Al_xN$ and wurtzite-structure AlN as confirmed by XTEM selected-area electron diffraction (SAED) results discussed below (see Figure 4(a)).

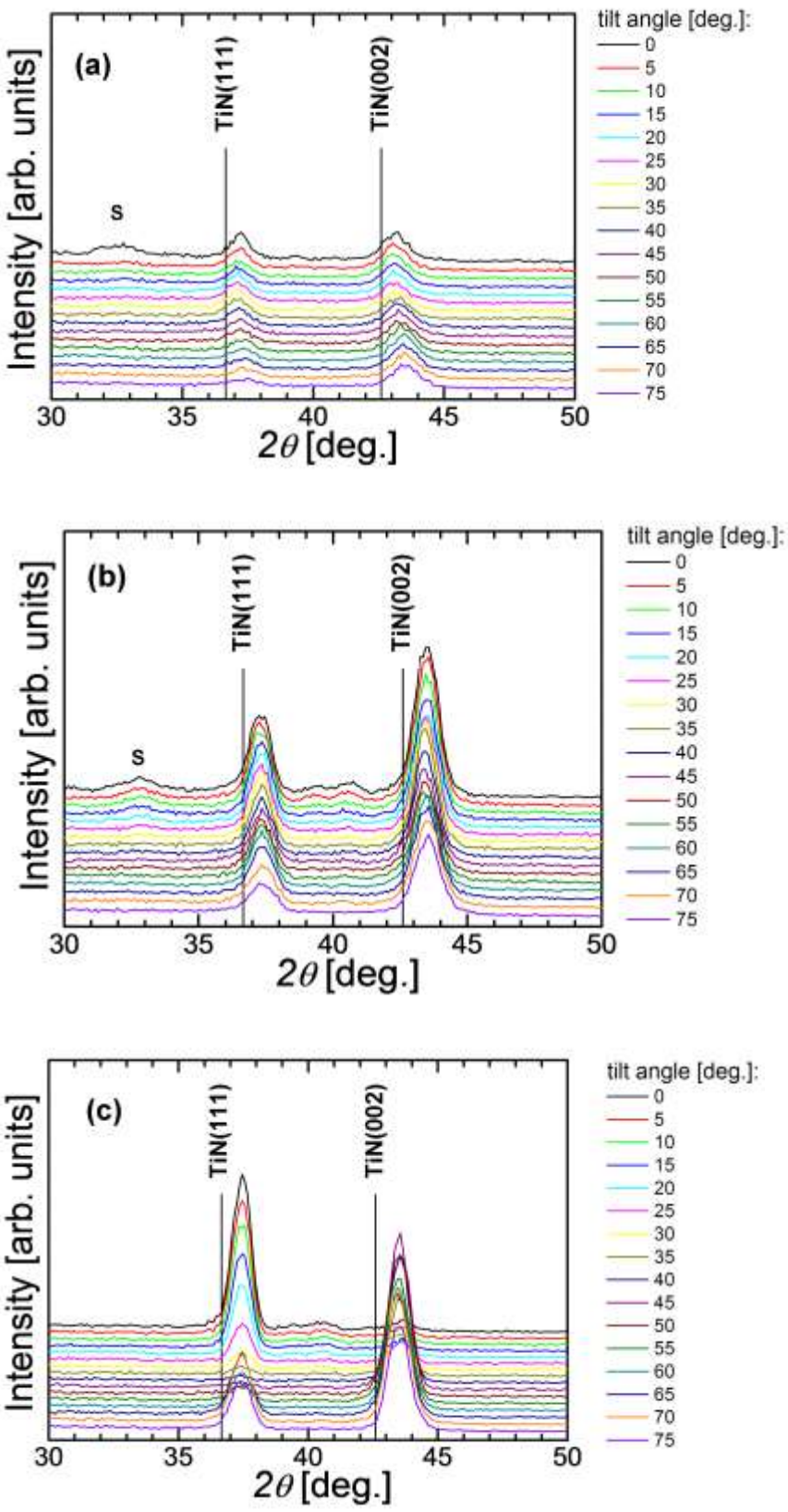

Fig.2 *ψ–2θ* scans as a function of tilt angle *ψ* (0° to 75° from top to bottom) for $Ti_{0.39}Al_{0.61}N$ alloy films deposited using one of three biasing schemes: (a) continuous DCMS bias; (b) synchronous bias applied during the full 200 μs HIPIMS pulse, and (c) bias applied in synchronous with the 60 μs metal-rich-plasma portion of the HIPIMS pulse.

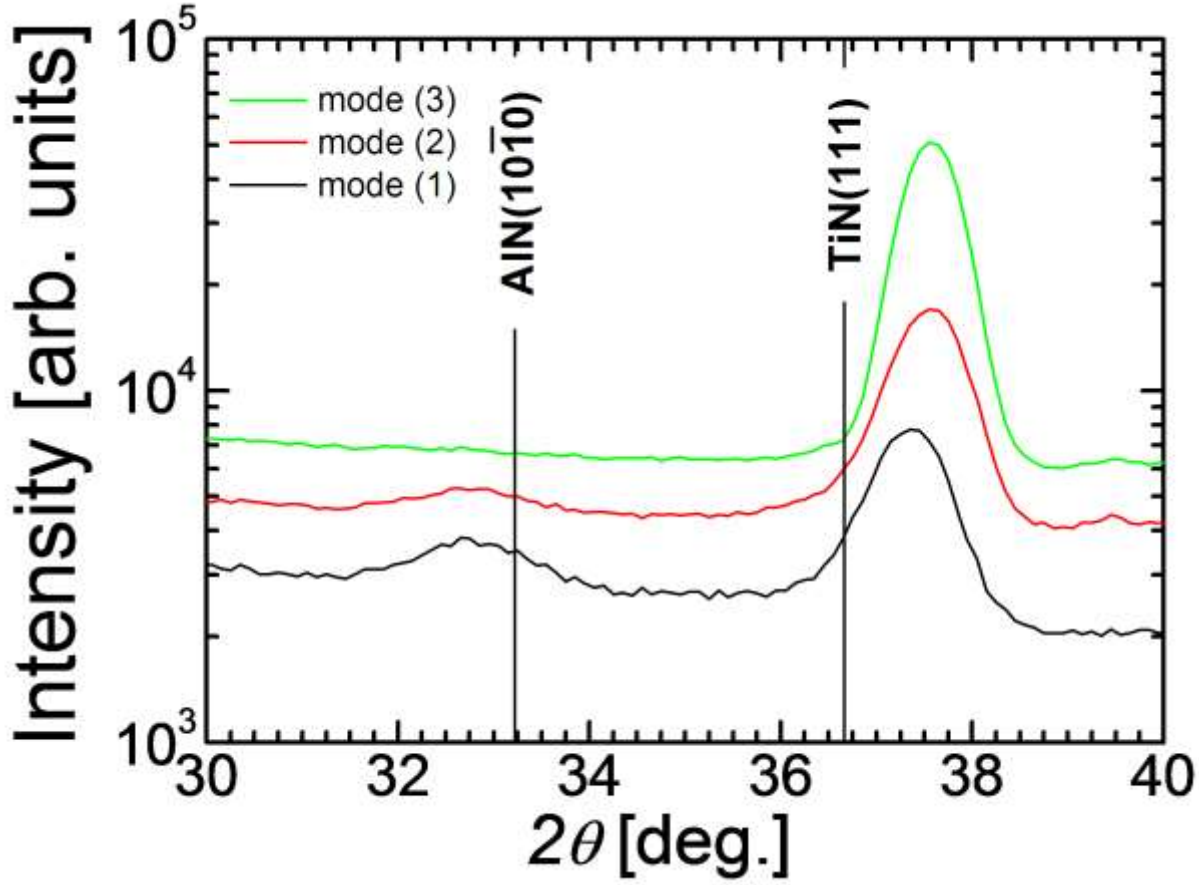

Fig.3 θ–2θ scans recorded at tilt angle ψ = 20° for $Ti_{0.39}Al_{0.61}N$ films deposited using one of three biasing schemes: (a) continuous DCMS bias (mode (1), bottom); (b) synchronous bias applied during the full 200 μs HIPIMS pulse (mode (2), middle), and (c) bias applied in synchronous with the 60 μs metal-rich-plasma portion of the HIPIMS pulse (mode (3), top).

Additional confirmation of the presence of *w*-AlN in mode (1) films is obtained from XRD scans (Figure 3) carried out with ψ = 20°, chosen in order to minimize the Si 002 substrate peak at 2θ = 32.96° (Ref. 13) which overlaps with the *w*-AlN 1010 peak at 33.22° (Ref. 14). The dwell time per data point is extended to 140 s in order to increase the signal-to-noise ratio. The *w*-AlN 1010 peak is observed, but shifted toward lower 2θ angles, 32.80°, indicating lattice expansion due to TiN incorporation into the hexagonal lattice.

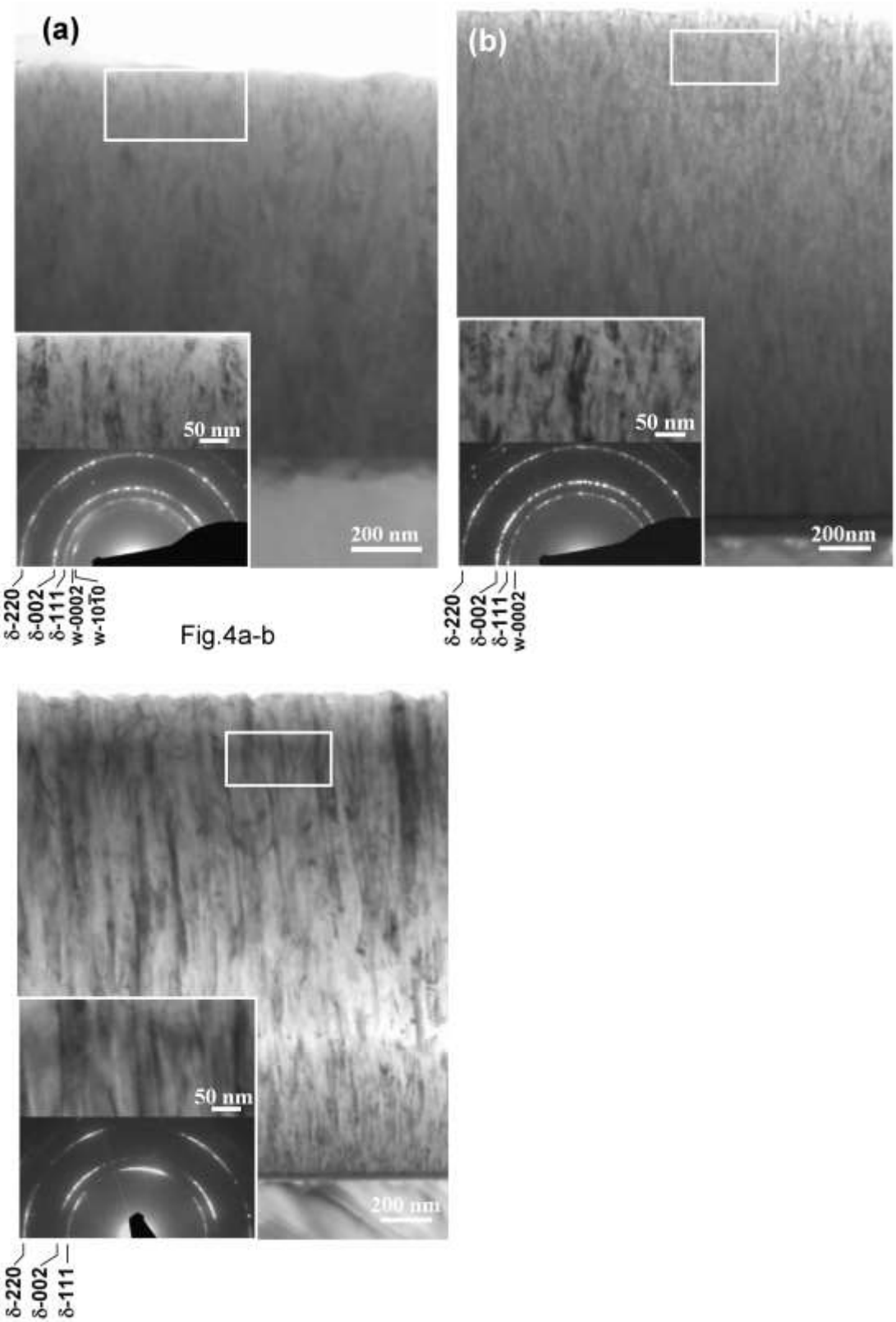

Fig.4a-b

Fig.4 XTEM images, including higher magnification expanded view and corresponding selected area diffraction pattern inserts, of $Ti_{0.39}Al_{0.61}N$ alloys deposited using one of three biasing schemes: (a) continuous DCMS bias; (b) synchronous bias applied during the full 200 μs HIPIMS pulse, and (c) bias applied in synchronous with the 60 μs metal-rich-plasma portion of the HIPIMS pulse.

Typical ψ-2θ XRD scans for $Ti_{0.39}Al_{0.61}N$ films grown under bias mode (2) are reproduced in Fig. 2(b). Here the bias is applied only during the 200 μs Al-HIPIMS pulses, corresponding to 10% of the total deposition time. For approximately one third of each HIPIMS pulse, the ion flux incident at the film is dominated by Al^+ (see Fig. 1), while Ar^+ is the primary bombarding ion during the remainder of the pulse. There is no applied bias during pure DCMS operation between the HIPIMS pulses.

The 111 and 002 peaks in the XRD scans from bias mode (2) films have intensities at ψ = 0° which are 3.4× higher than the corresponding peaks in mode (1) films, indicating a larger average grain size. The relaxed lattice parameter, a_o = 4.159 Å, is lower than for films grown under continuous dc bias and consistent with the expected value for predominately single phase x = 0.61 alloys.[7,11] A comparison of relative peak heights as a function of ψ reveals no strong preferred orientation. The corresponding 2θ scan, with ψ = 20° in Fig. 3, nevertheless reveals the presence of a small volume fraction of *w*-AlN; however, the intensity of the 1010 peak is lower than for mode (1) $Ti_{0.39}Al_{0.61}N$ layers. SAED patterns (see Fig. 4b) confirm the two-phase composition of mode (2) films.

Typical ψ-2θ XRD scans from mode (3) films, grown under synchronous bias during metal-mode HIPIMS, are presented in Fig. 2c. The NaCl-structure 111 peak intensity is 7.2× higher than for mode (1) films and ~ 2.4× higher than for mode (2) alloy films grown with t = 0-200 μs bias pulses. Moreover, the ratio of the relative 111/002 intensities and their evolution with increasing ψ reveals that mode (3) films have a strong 111 preferred orientation. The relaxed lattice parameter is 4.153 Å, consistent with single-phase x = 0.61 $Ti_{1-x}Al_xN$ alloys with a small N deficiency. In contrast to mode (1) and mode (2) layers, no *w*-AlN phase peak is detected in 2θ scans (Fig. 3). Mode (3) films are single-phase NaCl-structure $Ti_{0.39}Al_{0.61}N$ alloys.

Residual stress values σ for alloy films grown using each of the three bias modes are obtained from $\sin^2\psi$ analyses. For the randomly-oriented modes (1) and (2) films, we apply the procedure outlined in Ref. 15. Lattice spacings d_ψ are determined for each sample from the position of the 002 TiN Bragg reflection at 16 different values of the tilt angle ψ ranging from 0° and 75°. For the highly-oriented mode (3) films, we apply $\sin^2\psi$ analyses using a series of reflections belonging to the set of grains comprising the 111 fiber texture.[16] We measure the 111, 002, 022, 113, 133, and 024 *hkl* peak positions at ψ angles determined from the relationship

$$cos(\psi) = \frac{h+k+l}{\sqrt{3\left(h^2+k^2+l^2\right)}}. \qquad (1)$$

Elastic moduli *E*, required for obtaining σ values, are acquired from nanoindentation measurements analyzed accordingly to Ref. 17. Measured *E* values for modes (1), (2), and (3) films are 332, 427, and 377 GPa, respectively. Poisson's ratio, ν = 0.19, calculated for cubic $Ti_{1-x}Al_xN$ films with $0.5 \leq x \leq 0.75$, is obtained from Ref. 18.

Mode (1) films deposited under constant bias exhibit a large compressive stress, -3.4 GPa. For $Ti_{0.39}Al_{0.61}N$ layers grown using synchronized mode (2) and mode (3) bias schemes, σ is -0.2 GPa and +0.5 GPa, respectively. The measured stress values include a thermal contraction tensile stress σ_T due to the samples being cooled from T_s = 500 °C to room temperature. σ_T is given by[19]

$$\sigma_T = \frac{E\left(\alpha_f - \alpha_s\right)\Delta T}{1-\nu}, \qquad (2)$$

where $\alpha_s = 3\times10^{-6}$ K^{-1} is the expansion coefficient of Si, ΔT = 477 K, and α_f is the expansion coefficient of the alloy film, estimated as 9.35×10^{-6} K^{-1}.[20] Eqn. (2) yields σ_T = 1.2, 1.6, and 1.4 GPa for $Ti_{1-x}Al_xN$ films grown in modes (1), (2), and (3). Residual growth stresses corrected for thermal stress contributions are -4.6 for mode (1), -1.8 for mode (2), and -0.9

GPa for mode (3) films.

Typical XTEM results are presented in Fig. 4 for films grown using each of the three bias modes. SAED patterns and higher resolution images obtained from upper regions of the films, as indicated by white rectangles, are shown as insets. Fig. 4(a) reveals that mode (1) films consist of small grains (~200×200×200-500 $Å^3$) throughout the film thickness, elongated along the growth direction. This structure results from continuously recurring renucleation due to (i) residual damage from intense Ar^+ ion bombardment combined with (ii) the precipitation of incoherent *w*-AlN phase grains. Both effects interrupt local epitaxy. The corresponding SAED pattern consists of cubic $Ti_{1-x}Al_xN$ 111, 002, and 022, and wurtzite AlN 0002 and $10\bar{1}0$, diffraction rings. Uniform angular intensity of the diffracted signal is indicative of random orientation.

The nanostructure of mode (2) $Ti_{0.39}Al_{0.61}N$ layers, deposited using synchronized t = 0-200 μs pulsed bias (see Fig. 4(b)), is similar to that of mode (1) films, but with a larger grain size: 200-400 Å in width, extending 1000-1500 Å in the growth direction. The SAED pattern reveals 111, 002, and 022 cubic diffraction rings and a very weak *w*-AlN 0002 ring. Similar to mode (1) layers, there is again no indication of preferential orientation.

A distinctly different nanostructure is observed for mode (3) films (see Fig. 4(c)) grown with the bias pulse synchronized to the metal-ion portion of the HIPIMS pulse (t = 40-100 μs). The films consist of densely-packed columns, with no open boundaries, that extend throughout the entire film thickness. A pronounced competitive columnar growth occurs initially; the average column diameter, ~200 Å near the substrate, increases to 600-700 Å by the middle of the film, and 500-1000 Å near the film surface. Mode (3) films are single-phase NaCl-structure with no wurtzite signal detectable by either XRD or SAED. The 111 preferred orientation determined by XRD is also evident in XTEM SAED patterns as an increased 111 intensity in the film growth direction (see the inset in Fig. 4(c)), which is tilted with respect to

the surface normal by ~20° in the direction of the Al target.

IV. DISCUSSION

The incident ion energy E_i and ion-to-metal flux ratio J_i/J_{Me} are decisive parameters controlling nanostructural evolution during low temperature (< 500 ^{o}C; T_s/T_m < 0.3 for TiN) physical vapor deposition of transition metal (TM) nitrides by conventional reactive DCMS.[21,22,23,24,25,26,27] The dominant ion species incident at the growing film during DCMS with N_2/Ar gas mixtures optimized to obtain stoichiometric films is typically Ar^+, with N_2^+ and N^+ both contributing a few percent. The N_2^+/N^+ ratio increases with increasing N_2/Ar fraction, while in pure N_2 discharges the dominant ion species is N_2^+.[28] For magnetron sputtering, in which anode sheaths are of the order of ~1 mm, the ion energy E_i incident at the growing film corresponds closely to the applied negative substrate bias V_s.[21,22] That is, $E_i = e(V_s - V_{pl})$, where the plasma potential V_{pl} is typically ~3-5 V.[29]

Three polycrystalline TM nitride ion-assisted growth regimes have been identified.[19-25,28] (i) Under weak ion irradiation conditions ($J_i/J_{Me} \approx 1$; $E_i \approx 20$ eV) with low ion flux and ion energy, E_i is maintained below the bulk lattice atom displacement threshold. Film microstructure develops toward underdense columnar 111 texture via kinetically-limited competitive growth; adatoms have higher residence times on low-chemical-potential, low-diffusivity 111 planes. (ii) Increasing J_i/J_{Me} to ~5-10 while maintaining $E_i \approx 20$ eV, results in film densification. However, growth in regime (ii) remains competitive, but preferred orientation now evolves toward 002, rather than 111, texture. This is due to higher N coverage θ_N on 001 grains, resulting from N^+ adsorption and N_2^+ collisionally-induced dissociative chemisorption, dramatically decreasing metal cation mean-free paths, nucleation lengths L_{002}, and the 002 chemical potential μ_{002}.[25] 111 is a polar direction in NaCl-structure

nitrides for which the surface is always N-terminated; thus, the θ_N, L_{111}, and the chemical potential μ_{111} remain constant.[26] The resulting switch in chemical potential values, such that μ_{002} becomes less than μ_{111}, leads to the observed transformation in texture which now evolves to 002. Films grown in regimes (i) and (ii) exhibit no significant compressive stress.

A third regime (iii) of ion-assisted growth, which is widely utilized in conventional DC bias sputter deposition, is characterized by low ion densities, $J_i/J_{Me} \sim 1$, combined with relatively high ion energies, $E_i \sim 50$ eV, sufficient to generate linear cascade effects including recoil implantation and forward sputtering. This, in turn, leads to significant concentrations of trapped residual defects and a correspondingly high compressive stress. Dense 002 structures also develop under regime (iii). However, the mechanism for 002 texture formation is quite different than in regime (ii). In regime (iii), orientation evolves toward those planes which are least dense. Ion energy in open channel directions is distributed over larger depths yielding less lattice distortion and lower sputter yields. Therefore, planes orthogonal to open channel directions have higher survival probability. For film growth in this ion-assisted regime, several research groups have shown that the product of E_i and J_i/J_{Me} -- the average energy (E_d) per deposited atom -- can be correlated with film properties.[15,30,31,32]

Studies of nanostructural evolution and the phase stability of metastable $Ti_{0.5}Al_{0.5}N$ alloy films grown in regime (iii) have shown that with $E_d > 100$ eV/atom, ion irradiation results in precipitation of second-phase hexagonal AlN grains leading to $Ti_{1-x}Al_xN$ renucleation and a fine-grain two-phase nanostructure.[33] In addition to E_i and J_i/J_{Me}, momentum transfer to the growing film surface, controlled by the combination of ion/film atomic mass match and ion energy, as well as the chemical nature of the ion, inert gas *vs.* metal, are also expected to play an important role in controlling structural evolution. We focus particularly on these latter effects in the present experiments.

For $Ti_{0.39}Al_{0.61}N$ growth by Al-HIPIMS/Ti-DCMS deposition, the average energy per deposited atom delivered to the film growth surface, including that provided by the DCMS plasma, during an entire τ = 2 ms period, is

$$\left\langle \overline{E}_d \right\rangle = \frac{1}{\tau}\int_0^{\tau} E_i(t)\left(J_i/J_{Me}\right)(t)\,dt\,. \qquad (2)$$

In our experiments, J_i/J_{Me}(HIPIMS) ~ J_i/J_{Me}(DCMS) ~ 3.1; hence, $\left\langle \overline{E}_d \right\rangle$ is primarily determined by the time-averaged energy of incident ions, $\left\langle E_i \right\rangle = \frac{1}{\tau}\int_0^{\tau} E_i(t)\,dt$.

The substrate bias, V_s = -60 V, is applied during 100% of the deposition time (mode 1), 10% (mode 2), and 3% (mode 3). For the remaining deposition time, in modes (2) and (3), the growing films are at floating potential V_f ~ -10 V. Using the mean ion energies and relative contributions to the total ion flux obtained from the *in-situ* ion mass spectrometry analyses, $\left\langle \overline{E}_d \right\rangle = \left\langle E_i \right\rangle \times J_i/J_{Me}$ is approximately 200 eV/atom for continuous DC bias (mode 1), 55 eV/atom for the full 200 μs HIPIMS pulse (mode 2), and 45 eV/atom in the case for which the bias pulse is synchronized with the metal-rich portion of the high-power pulse (mode 3).

During mode (1) growth, ion irradiation with $\left\langle \overline{E}_d \right\rangle$= 200 eV/atom results in the precipitation of a significant mole fraction of second-phase *w*-AlN, as evident from both XRD (Fig. 3) and SAED results (Fig. 4(a)). Intense uninterrupted Ar^+ ion bombardment, with incident fluxes 3× that of the deposited metal, leads to large transient, and smaller residual, defect concentrations. The transient defect flux derives from local microscopic compressive stress driving implanted Ar and excess recoil-implanted lattice atoms toward the surface in order to partially relax the lattice.

The combination of transient and the residual trapped defects destabilizes the metastable NaCl structure and facilitates the precipitation of second phase *w*-AlN. This, in turn, disrupts local epitaxial growth on cubic NaCl-structure grains. The resulting continuous renucleation gives rise to the formation of a randomly-oriented, thickness-invariant, fine-grain (~200×200×200-500 $Å^3$) nanostructure, with grains slightly elongated in the growth direction. The intense Ar^+ ion irradiation during mode (1) growth also results in extensive material loss by resputtering, predominantly during the DCMS phase, leading to thinner films for a fixed deposition time. The presence of residual trapped Ar, 0.2 at%, and ion-induced defects explain the observed high compressive stress, -4.6 GPa.

$\langle \overline{E}_d \rangle$ is reduced to 55 eV/atom during mode (2) growth; thus, there is less resputtering and thicker films are obtained. The correspondingly lower defect densities result in less renucleation; hence, the average grain size is larger (~300×300×1000-1500 $Å^3$), with grains more elongated in the growth direction, and the volume fraction of *w*-AlN second phase precipitates is lower. The incorporated Ar concentration is below detection limits and the residual stress is significantly decreased to -1.8 GPa.

In mode (3) film growth, for which $\langle \overline{E}_d \rangle$ = 45 eV/atom, $Ti_{0.39}Al_{0.61}N$ layers are single-phase, local epitaxy is uninterrupted, and the films exhibit a columnar nanostructure (see Fig.4(c)) in which the average column width *w* increases with film thickness *h*. During the early stages of mode (3) growth, films exhibit a randomly oriented, fine-grain equiaxed structure (~200×200×200 A^3), from which, unlike layers grown in modes (1) and (2), a kinetically-limited 111 texture slowly evolves. The average column width *w* increases with film thickness *h*, giving rise to V-shaped columns with diameters of 500-1000 Å at the surface, *h* = 1.9 μm. The 111 texture emerges due to larger adatom residence times on low-potential-energy 111, than 002, surfaces.[22,26] Residual defect concentrations, and hence

residual stress (-0.9 GPa), is lower under Al^+, rather than Ar^+, ion irradiation since Al is primarily incorporated into the lattice of the growing film, whereas Ar resides in interstitial sites resulting in compressive stress. The 111 columnar structure is fully dense, with no observable intra- and intercolumnar voids. Thus, Al^+ irradiation with $\langle \overline{E}_d \rangle$ = 45 eV/atom and $J_i/J_{Me} \sim 3$ results in sufficient lattice atom displacements (through recoil implantation and forward sputtering) to eliminate the voids typically observed in low-temperature ($T_s/T_m \leq$ 0.3) TM nitride films.[21,23,24,26,27]

The relatively small decrease in $\langle \overline{E}_d \rangle$ from 55 eV/atom for mode (2) to 45 eV/atom for mode (3) films can not entirely explain the dramatic nanostructural differences observed in the two cases. Instead, we attribute most of the difference to the fact that the majority of energetic ions incident at the growing film surface are Al^+ during mode (3), *vs*. Ar^+ ions in mode (2) growth, due to substrate bias synchronization with the metallic portion of the HIPIMS pulses. There are at least two reasons which can be proposed for this: differences in momentum transfer to the growing film and, as noted above, the fact that Al is incorporated in lattice sites, while Ar is incorporated as interstitials.

Momentum transfer Φ between an incident ion with mass m_i and the film with average mass m_f is given by $\Phi = 4m_f m_i/(m_f + m_i)^2$ for 180° hard-sphere collisions. Here, m_i = 26.98 amu and 39.95 amu for Al^+ and Ar^+, while m_f = 24.5 amu. Thus, Φ = 0.998 for Al^+ irradiation and 0.944 for Ar^+ bombardment.[34] This difference is too small to account for the dramatic change in nanostructure observed between modes (2) and (3) films.

Thus, the primary difference in nanostructural evolution results from the chemical nature of the ions – inert gas *vs.* constituent metal ions. With $J_i/J_{Me} \sim 3$ and $E_i \approx 70$ eV, there is a large dynamic concentration of implanted near-surface Ar during mode (2) $Ti_{0.39}Al_{0.61}N$ growth. Most of the implanted Ar diffuses back to the surface, driven by compressive strain,

with a migration rate enhanced by high ion-induced near-surface defect concentrations. Thus, there are continuous opposing Ar implantation and out-diffusion fluxes during film growth. This high transient defect concentration, together with the trapped residual defects, destabilizes the metastable NaCl-structure host lattice resulting in second-phase *w*-AlN precipitation, loss of local epitaxy, and the formation of the fine-grained randomly-oriented nanostructure observed in both modes (1) and (2) films.

Energetic Al^+ ions cause sufficient lattice-atom displacements to eliminate film porosity. However, Al, as opposed to Ar, is primarily incorporated in lattice sites, as indicated by the low stress, and does not result in nucleation of *w*-AlN. Mode (3) films have a dense, columnar, 111 oriented microstructure which is not attainable in regimes (i)-(iii) of standard bias magnetron reactive sputtering for which the structure varies from underdense 111 to dense 002.

Applying a pulsed bias synchronized with the metal-rich plasma opens a new pathway for microstructure evolution and control which is a combination of regimes (i) and (iii). The (111) texture evolves through kinetically-limited competitive growth following the development of a fine-grained randomly-oriented structure during the nucleation, coalescence, and early stages of film growth. The 111 columns, whose average widths increase with film thickness, slowly win the growth competition due to higher adatom residence times on low-chemical-potential, low-diffusivity 111 planes. Similar to growth regime (iii), the bombarding Al^+ ions have sufficient energy to penetrate the lattice and cause densification via forward momentum transfer in shallow overlapping cascades. However, Al^+ ions are primarily incorporated at lattice sites, do not result in high residual defect concentrations, and thus preserve local 111 epitaxial growth.

V. CONCLUSIONS

In summary, we demonstrate that the use of a synchronous pulsed bias during hybrid HIPIMS/DCMS co-sputter deposition of $Ti_{1-x}Al_xN$ decreases, or eliminates, depending on whether the bias is applied during the entire HIPIMS pulse or only during the metal ion phase, the compressive stress associated with trapped rare gas. Alloy films grown with continuous dc bias are small-grain, two-phase mixtures, consisting of AlN-deficient NaCl-structure $Ti_{1-x}Al_xN$ and wurtzite-structure AlN, with high compressive stress, a large concentration of trapped Ar, and no preferred crystallographic orientation. Synchronizing the bias with the full HIPIMS pulse to the Al target results in films which have significantly lower compressive stress with no measureable Ar incorporation, larger average grain size, a smaller volume fraction of wurtzite AlN, and random texture. In contrast, by synchronizing the bias with the metal plasma phase of the HIPIMS pulses, high-energy Ar^+ ion irradiation is greatly reduced in favor of irradiation predominantly by Al^+ ions. The resulting single-phase NaCl-structure $Ti_{0.39}Al_{0.61}N$ alloys have a dense columnar structure with a strong 111 orientation and are nearly stress-free.

ACKNOWLEDGEMENTS

The financial support from the Swedish VINN Excellence Center on Functional Nanoscale Materials (FunMat) is acknowledged. We thank the staff at the Tandem Laboratory, Uppsala University, for technical support.

[1] D. McIntyre, J.E. Greene, G. Håkansson, J.-E. Sundgren, W.-D. Munz *Oxidation of Metastable Single-phase Polycrystalline $Ti_{0.5}Al_{0.5}N$ Films: Kinetics and Mechanisms* J. Appl. Phys. **67**, 1542-53 (1990).
[2] O. Knotek, M. Böhmer, T. Leyendecker *On Structure and Properties of Sputtered Ti and Al Based Hard Compound Films* J. Vac. Sci. Technol. A **4**, 2695 (1986).
[3] F. Adibi, I. Petrov, L. Hultman, U. Wahlström, T. Shimizu, D. McIntyre, J.E. Greene J. Appl. Phys. **69**, 6437 (1991).
[4] J.S. Schuster and J. Bauer, J. Solid State Chem. **53**, 260 (1984).
[5] H. Holleck, Surf. Coat. Tech. **36**, 151 (1988).
[6] G. Greczynski, J. Lu, M. Johansson, J. Jensen, I. Petrov, J.E. Greene, and L. Hultman *Selection of Metal Ion Irradiation for Controlling $Ti_{1-x}Al_xN$ Alloy Growth via Hybrid HIPIMS/magnetron Co-sputtering*, Vacuum **86**, 1036 (2012).
[7] G. Greczynski, J. Lu, M. Johansson, J. Jensen, I. Petrov, J.E. Greene, and L. Hultman, *Role of Ti^{n+} and Al^{n+} Ion Irradiation (n = 1, 2) During $Ti_{1-x}Al_xN$ Alloy Film Growth in a Hybrid HIPIMS/magnetron Mode*, Surf. Coat. Tech. **206**, 4202 (2012).
[8]http://www.cemecon.de/coating_technology/2_coating_units/25_cc_800sup_sup_9_hipims/index_eng.html, accessed in September, 2011.
[9]See, for example, Chapter 6 in M. Birkholz *Thin Film Analysis by X-ray Scattering*, Wiley-VCH, Weinheim (2006).
[10] David R. Lide (ed), *CRC Handbook of Chemistry and Physics, 84th Edition*. CRC Press. Boca Raton, Florida, 2003; Section 10, Atomic, Molecular, and Optical Physics; Ionization Potentials of Atoms and Atomic Ions.
[11] F. Adibi, I. Petrov, J. E. Greene, U. Wahlström, and J.-E. Sundgren, *Design and Characterization of a Compact Two-Target Ultrahigh Vacuum Magnetron Sputter Deposition System: Application to the Growth of Epitaxial $Ti_{1-x}Al_xN$ alloys and $TiN/Ti_{1-x}Al_xN$ Superlattices*, J. Vac. Sci. Technol. A, **11**, 136 (1993).
[12] B. Alling, A. Karimi, I.A. Abrikosov *Electronic Origin of the Isostructural Decomposition in Cubic $M_{1-x}Al_xN$ (M=Ti, Cr, Sc, Hf): A First-principles Study* Surf. Coat. Tech. **203**, 883 (2008).
[13] Although the Si 002 reflection is forbidden by extinction rules, it can appear due to multiple scattering.
[14] The JCPDS database (1998), card: 25-1133; Kohn et al. Am. Mineral **41**, 355 (1956).
[15] J. Musil, S. Kadlec, V. Valvoda, R. Kuzel, and R. Cerny, Surf. Coat. Tech. **43/44**, 259 (1990).
[16] Y.-W. Kim, J. Moser, I. Petrov, J. E. Greene, and S. M. Rossnagel, *Directed Sputter Deposition of AlCu: Film Microstructure and Microchemistry*, J. Vac. Sci. Technol. A, **12**, 3169 (1994).
[17] W. C. Oliver and G. M. Pharr, J. Mater. Res. **7**, 1564 (1992).
[18] V. Podgursky *Ab initio Calculations of Elastic Properties of Isotropic and Oriented $Ti_{1-x}Al_xN$ Hard Coatings* J. Phys. D: Appl. Phys. **40**, 4021 (2007).
[19] See, for example, M. Ohring, *Materials Science of Thin Films*, 2nd edition, Academic Press, 2001, p. 732-733.
[20] Here, we use α_f for TiN since there are no published values for $Ti_{0.39}Al_{0.61}N$. We expect α_f to be larger for the alloy; hence, σ_T values obtained from eqn. (2) are lower limits.
[21] I. Petrov, F. Adibi, J. E. Greene, L. Hultman and J.-E. Sundgren, *Average Energy Deposited per Atom: A Universal Parameter for Describing Ion-Assisted Film Growth?*, Appl. Phys. Lett. **63**, 36 (1993).
[22] J. E. Greene, J.-E. Sundgren, L. Hultman, I. Petrov, and D. B. Bergstrom, *Development of Preferred Orientation in Polycrystalline TiN Layers Grown by Ultra-High-Vacuum Reactive Magnetron Sputtering*, Appl. Phys. Lett. **67**, 2928 (1995).
[23] I. Petrov, P.B. Barna, L. Hultman, J.E. Greene *Microstructural Evolution During Film Growth* J. Vac. Sci. Technol. A **21**, 117 (2003).
[24] C.-S. Shin, Y.-W. Kim, D. Gall, J. E. Greene, and I. Petrov, *Phase Composition and Microstructure of Polycrystalline and Epitaxial TaN_x Layers Grown on oxidized Si(001) and MgO(001) by Reactive Magnetron Sputter Deposition*, Thin Solid Films **402**, 172 (2002).
[25] D. Gall, C.-S. Shin, T. Spila, M. Odén, M. J. H. Senna, J. E. Greene, and I. Petrov, *Growth of Single-crystal CrN on MgO(001): Effects of Low-energy Ion-irradiation on Surface Morphological Evolution and Physical Properties* J. Appl. Phys. **91**, 3589 (2002).
[26] D. Gall, I. Petrov, N. Hellgren, L. Hultman, J.-E. Sundgren, and J. E. Greene, *Growth of Poly- and Single-Crystal ScN on MgO(001): Role of Low-Energy N_2^+ Irradiation in Determining Texture, Microstructure Evolution, and Mechanical Properties*, J. Appl. Phys. **84**, 6034 (1998).
[27] D. Gall, I. Petrov, and J. E. Greene, *Epitaxial Sc1-xTixN(001: Optical and Electronic Transport Properties*, J. Appl. Phys., **89**, 401 (2001).

[28] I. Petrov, A. Myers, J. E. Greene, and J. R. Abelson, *Mass and Energy Resolved Detection of Ions and Neutral Sputtered Species Incident at the Substrate during Reactive Magnetron Sputtering of Ti in Mixed Ar+N2 Discharges*, J. Vac. Sci. Technol. A, **12**, 2846 (1994).

[29] I. Petrov, F. Adibi, J. E. Greene, W. D. Sproul and W.-D. Münz, *Use of an Externally Applied Axial Magnetic Field to Control Ion/Neutral Flux Ratios Incident at the Substrate During Magnetron Sputter Deposition*, J. Vac. Sci. Technol. A, **10**, 3283 (1992).

[30] J. M. E. Harper, J. J. Cuomo, R. J. Gambino, and H. R. Kaufman, in Ion Bombardment Modification of Surfaces, edited by 0. Auciello and R. Kelly (Elsevier, New York, 1984). Chap. 4.

[31] T. C. Huang, G. Lim, F. Parmigiani, and E. Kay, J. Vac. Sci. Technol. A **3**, 2161 (1985).

[32] J. E. Yehoda, B. Yang, K. Vedam, and R. Messier, J. Vac. Sci. Technol. A **6**, 1631 (1988).

[33] F. Adibi, I. Petrov, J. E. Greene, L. Hultman, and J.-E. Sundgren, *Effects of High Flux Low-Energy (<50 eV) Ion Irradiation During Deposition on the Microstructure and Preferred Orientaion of $Ti_{0.5}Al_{0.5}N$ Alloys Grown by UHV Reactive Magnetron Sputtering*, J. Appl. Phys. **73**, 8580 (1993).

[34] The values for energetic Ar^+ and Al^+ impinging on Ti, Al, and N are 0.992, 0.962 ,and 0.768, and 0.920, 1, and 0.899, respectively.